

Original Research Article: Temperature's Impact on the Physical Properties of Rare Earth Element Doped SrS for Optoelectronic Use

Shaka Oghenemega Samuel¹, Zhimwang Jangfa Timothy², Clever Kate Ojoba³, Imosobomeh Lucky Ikhioya^{4, 5*}

¹Department of Science Laboratory Technology, Delta State University, Abraka, Delta State, Nigeria

²Federal University of Lokoja, Lokoja, Nigeria

³Department of Physics, College of Education Warri, Delta State, Nigeria

⁴Department of Physics and Astronomy, University of Nigeria, Nsukka, Enugu State, Nigeria

⁵National Centre for Physics, Quaid-i-Azam University Campus, Islamabad, Pakistan

Use your device to scan and read the article online



Citation S.O. Samuel, Z.J. Timothy, C.K.O joba, I.L. Ikhioya*. **Temperature's Impact on the Physical Properties of Rare Earth Element Doped SrS for Optoelectronic Use.** *J. Eng. Ind. Res.* 2023, 4 (3):147-156.

 <https://doi.org/10.48309/IEIRES.2023.3.2>



Article info:

Received: 2023-10-03

Accepted: 2023-11-24

ID: JEIRES-2311-1099

Checked for Plagiarism: Yes

Editor who Approved Publication:

Fatimah Ramezani

Keywords:

XRD; Optical; EDX; Optoelectronic; Bandgap; SEM.

ABSTRACT

In this research, SrS/Zr material was synthesized using the concentrations of 0.1 mol of strontium chloride hexahydrate (SrCl₂·6H₂O), 0.01 mol of Zirconium (IV) oxychloride octahydrate (ZrOCl₂·8H₂O), and thioacetamide (C₂H₅NS). The spectrum is polycrystalline with a cubic structure and a noticeable (111) peak. The addition of 0.01 mol of zirconium dopant increases the peak intensity, confirming successful doping. Precursor temperature affects peak intensity, indicating film crystallinity. The spectrum is cubic with a distinct (111) peak and is polycrystalline. Peak intensity rises with the addition of 0.01 mol zirconium dopant, implying dopant acceptance. Peak intensity grows with higher precursor temperature, showing film crystallite. Cloudlike precipitates appear on the film surface because of variations in precursor temperature. The cloudlike precipitate recircled and created a dense cloud on the film surface with increasing precursor temperature. The SrS material with doping showed consistent deposition and complete substrate coverage by nanoparticles for photovoltaic applications. The synthesized films have an energy bandgap of 1.23 eV to 1.50 eV.

Introduction

Industries such as semiconductors and optical coatings have benefited from thin film deposition techniques over the past century [1]. Some applications include thin-film solar cells, LEDs, and magnetic recording media. Thin films can benefit the study of unique materials like super-lattices

and multiferroic materials, enabling experiments in quantum confinement and two-dimensional electron states. The remarkable growth of storage, micro-electromechanical systems, chip interconnects, and microelectronic packaging can be attributed to the advancements in electrodeposition [2].

*Corresponding Author: Imosobomeh L. Ikhioya (imosobomeh.ikhioya@unn.edu.ng)

Because of increasing global demand, particularly in developed and developing nations, more sustainable energy solutions are now needed to replace traditional electrical generation resources such as fossil fuels [3]. Fossil fuel-based energy sources are to blame for damaging environmental problems like climate change and global warming [4]. In the last several decades, the amount of Green-house gases released into the environment during the electricity production has drastically increased [4].

Renewable energy technologies like solar, wind, hydro, biomass, geothermal, and hydrogen are being used to combat the environmental crisis [5-8]. Alternative energy is gaining more and more attention as a result of their environmentally favorable qualities and capacity to produce electricity with zero or almost zero emission of air pollutants [9-14], as societal awareness of the importance of a clean environment rises. RE provides economic value in addition to contributing to sustainability. Because it produces energy from natural, renewable resources, it helps the economy by lowering the cost of electricity generation [15-17].

In addition, since users can sell the electricity they generate back to the power grid, it can be a secondary source of revenue. Because of the intermittent nature of alternative energy and its high initial cost, even if the adoption of alternative energy sources for power generation is growing, the majority of power is still produced using fossil fuels. For instance, a solar system can only be utilized during the day, a wind turbine can only be used when there is enough airflow, and a hydro turbine can only be used when water flow is creating potential energy. Scientists are working hard to improve the effectiveness and address the drawbacks of alternative energy.

Strontium sulphide is one of the most well-known and important compounds in the family of alkaline-earth sulphides. Many groups have studied how the energy gap, phonon spectrum, optical properties, structural phase stability, elastic properties, and metallization process

vary with volume. The most stable form of strontium sulphide at room temperature is the rock-salt phase, according to their findings. Alkaline-earth sulphide is used as the host material in devices like multicolor thin-film electroluminescent devices and magneto-optical systems [15].

An important approach to consider is the electrochemical deposition method. The combination of atypical metals with comparable properties alongside layers of affordable, readily available base materials. Their range of application now covers tasks that would have been impossible in different circumstances [18-20].

Electrochemical deposition was used to achieve the synthesis of SrS-doped zirconium materials at different precursor temperatures in this study. The film structure, morphology, elemental content, and electrical properties were examined via reliable characterization tools.

Materials

These are the materials used in the study: strontium chloride hexahydrate ($\text{SrCl}_2 \cdot 6\text{H}_2\text{O}$) Sigma-Aldrich 99.9%, Zirconium (IV) oxychloride octahydrate ($\text{ZrOCl}_2 \cdot 8\text{H}_2\text{O}$) Sigma-Aldrich 99.9%, Thioacetamide ($\text{C}_2\text{H}_5\text{NS}$) Sigma-Aldrich 99.9%, deionized water, heating mantle, FTO-fluorine-doped tin oxide substrate, and oven with a temperature range of 50 to 1000 °C.

Synthesis of SrS and SrS/Zr

Analytically evaluated chemicals are purchased and immediately utilized. The experimental setup involved using FTO substrate. The FTO was cleaned using distilled water, then immersed in methanol and acetone, and finally treated with acetone for 40 minutes. The cleaning process involved using distilled water and then drying. The concentrations used were 0.1 mol of strontium chloride hexahydrate ($\text{SrCl}_2 \cdot 6\text{H}_2\text{O}$), 0.01 mol of Zirconium (IV) oxychloride octahydrate ($\text{ZrOCl}_2 \cdot 8\text{H}_2\text{O}$), and thioacetamide ($\text{C}_2\text{H}_5\text{NS}$). The electrochemical deposition process was used to deposit the

films. In the electrochemical apparatus, the bath comprised DH_2O , 20 ml of cationic and anionic material each, and a 100 ml beaker. The FTO substrate and carbon served as the cathode and anode materials, respectively, while the power supply generated DC. In the chamber, there are (3) electrode configurations: a working electrode, a reference electrode (Ag/AgCl), and a positive electrode made of platinum mesh. The FTO was positioned perpendicular to the chamber in all depositions, alongside the reference and counter electrodes. The synthesis took place with a potentiostat set at 200 mV against SCE for 10 seconds. Consequently, the synthesized films underwent a cleaning and drying process. During the deposition procedure, the beakers were filled with the target materials (20 ml each of strontium chloride, thioacetamide, and 10 ml of Zirconium (IV) oxychloride octahydrate solution).

The films were heated and annealed for 30 minutes after the syntheses to release the accumulated tension. The zirconium dopant was introduced by adding 10 ml of 0.01 mol to the electrochemical bath. The pH levels for sample collection were 7.0 and the precursor temperature varied between 35, 40, and 45 °C. The elemental, electrical, structural, surface

morphological, and optical properties of the prepared SrS and SrS/Zr films were assessed using a UV-1800 visible spectrophotometer, a four-point probe (Model T345), scanning electron microscopy, and DW-XRD 2700A X-ray diffractometer with $\text{Cu-K}\alpha$ line ($\lambda = 1.54184 \text{ \AA}$) in 2θ range from 10° - 80° .

Results and Discussion

Analysis of resistivity and conductivity of SrS and SrS/Zr

Table 1 presents the resistivity and conductivity values for SrS and SrS/Zr. The films show a decrease in thickness from 125.02 to 102.03 nm, along with an increase in resistivity ranging from 1.31×10^9 to $1.39 \times 10^9 \text{ ohm.m}$, resulting in a subsequent decrease in conductivity ranging from 7.57×10^8 to $7.19 \times 10^8 \text{ S/m}$. The synthesized films had good conductivity, making them useful for photovoltaics and solar cells. Figure 1 (a) illustrates the correlation between reduced film thickness and increased conductivity, as evidenced by low resistivity. Figure 1 (b) illustrates the nonlinear relationship between resistivity, conductivity, and precursor temperature, showcasing the increase and decrease patterns.

Table 1: Electrical parameters of SrS and doped SrS with zirconium

Film	t (nm)	ρ ($\Omega\cdot\text{m}$)	σ (S/m) ⁻¹
SrS pristine	125.02	1.32×10^9	7.57×10^8
SrS/Zr 35 °C	123.08	1.31×10^9	7.63×10^8
SrS/Zr 40 °C	123.09	1.36×10^9	7.35×10^8
SrS/Zr 45 °C	102.03	1.39×10^9	7.19×10^8

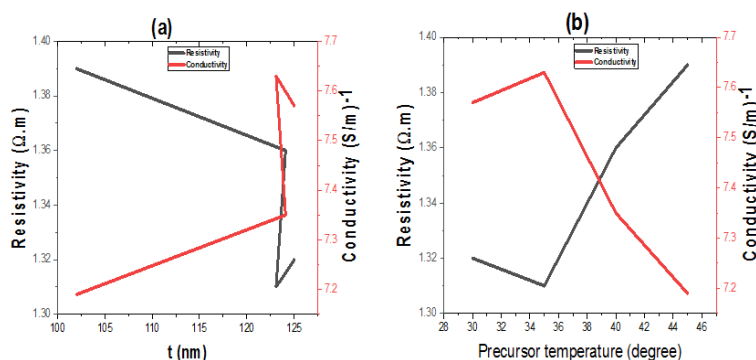


Figure 1: Resistivity and conductivity vs. thickness (a), and precursor temperature (b)

XRD study on SrS and Zr-doped SrS

The spectrum of SrS and SrS doped zirconium at various precursor temperatures is depicted in Figure 2. The spectrum's cubic-structure includes a significant peak at orientation (111) and is polycrystalline. The peak intensity increases with 0.01 M of zirconium dopant addition, indicating that the precursor has accepted the dopant.

Higher precursor temperature causes the peak intensity to grow, which indicates the crystallite of the films; the substrate used for the deposition causes an unindexed peak to appear. Polycrystalline materials are always more advantageous for creating optoelectronic devices because of their nature. The spectrum indicates that the peak intensities of the synthesized material will increase with a

greater precursor temperature. The crystallite size of the films is also listed in Table 2, along with the calculated crystallite sizes, dislocation density, and precursor temperature. Figure 2b displays the value of $(\beta \cos \theta \text{ vs. } \sin \theta)$. The slope of the Williamson-Hall (W-H) plot decreases with increasing precursor temperature.

Higher precursor temperature leads to changes in crystal size, dislocation density, and diffraction angle peak because of strain hardening. In Figure 2c, the plot displays the relationship between the crystallite size of the deposited material and the 2-theta. As 2theta increases, the material decreases, which is different from the temperature-dependent change observed before. The diffraction angle increases with decreasing crystallite size.

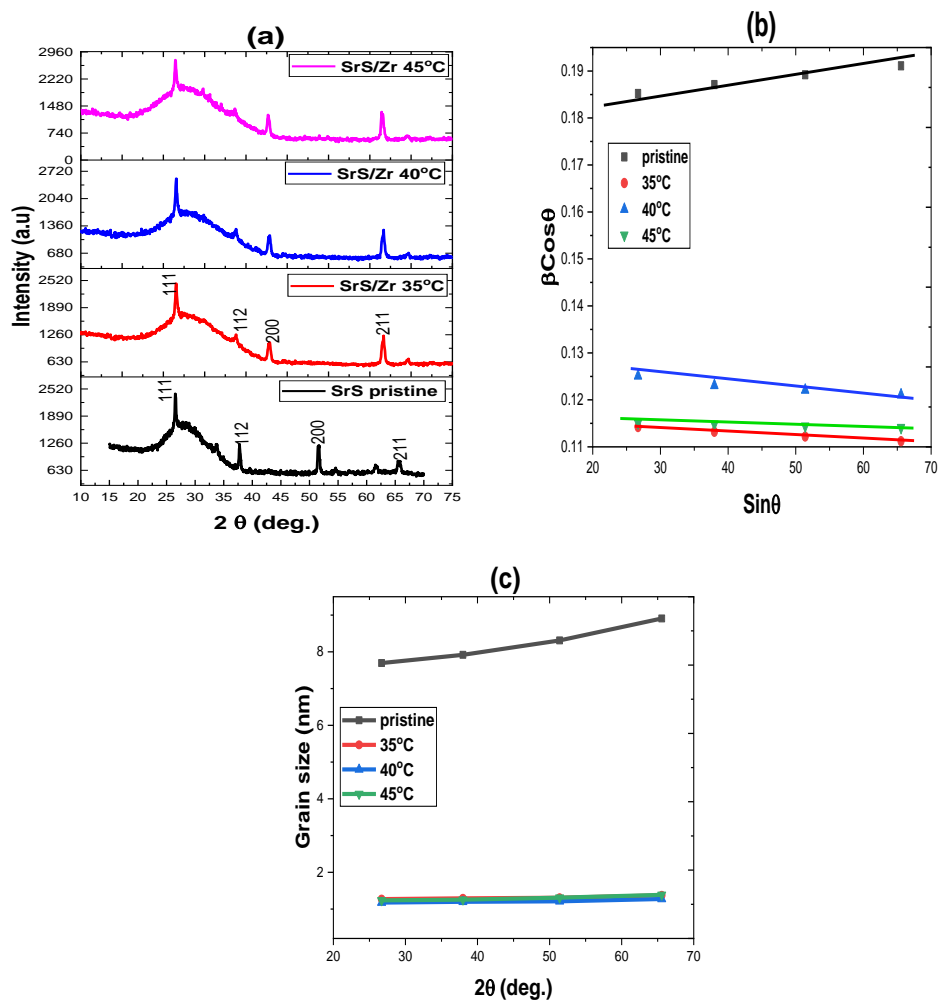


Figure 2: XRD pattern [a], W-H plot [b], and crystallite size Vs 2-theta [c]

Table 2: Structural parameters of SrS/Zr

Films	2 θ (deg.)	d (spacing) Å	(Δ)	(β)	(hkl)	(D) nm	σ lines/m ²
SrS pristine	26.6971	3.3360	5.7781	0.1852	111	7.6958	5.1445
	37.9741	2.3672	4.7345	0.1871	112	7.9188	4.9700
	51.3944	1.7762	3.5524	0.1892	200	8.3100	4.8648
	65.5611	1.4225	3.1809	0.1911	211	8.9066	4.3940
SrS/Zr 35 °C	26.7313	3.3318	5.7709	0.1142	111	1.2701	1.8881
	33.7975	2.6496	5.2992	0.1132	112	1.2915	1.8261
	37.9481	2.3688	4.7376	0.1122	200	1.3067	1.7838
	51.8061	1.7630	3.9423	0.1112	211	1.3738	1.6140
SrS/Zr 40 °C	26.7313	3.3318	5.7709	0.1251	111	1.1768	2.1995
	33.7975	2.6496	5.2992	0.1231	112	1.1966	2.1273
	37.9481	2.3688	4.7376	0.1221	200	1.2107	2.0780
	51.8061	1.7630	3.9423	0.1211	211	1.2728	1.8802
SrS/Zr 45 °C	26.7313	3.3318	5.7709	0.1151	111	1.2377	1.9414
	33.7975	2.6496	5.2992	0.1148	112	1.2559	1.78676
	37.9481	2.3688	4.7376	0.1144	200	1.3102	1.5913
	51.8061	1.7630	3.9423	0.1141	211	1.3872	1.4405

Analysis of SrS and SrS/Zr materials' optical behavior

Figure 3 (a) shows the absorbance of SrS doped zirconium at various precursor temperatures. The spectrum shows a cubic structure, with a distinct (111) peak and polycrystalline nature. The precursor's acceptance of the dopant is indicated by the increase in peak intensity with the addition of 0.01 mol of zirconium. The peak intensity increases with higher precursor temperature, indicating film crystallinity. SrS/Zr has higher absorbance and is a better choice for photovoltaic cells and energy storage. The transmittance of SrS and SrS-doped zirconium is depicted in Figure 3 (b).

The film's transmittance increased as the wavelength of light radiation increased. The films are greatly affected by the zirconium dopant and precursor temperature. Increasing the precursor temperature also increases the film's transmittance. Doping SrS with zirconium enhances the transmittance of the synthesized material. The SrS/Zr transmittance decreases

with a higher precursor temperature. SrS/Zr has a higher transmittance, making it a superior material for photovoltaic cells and energy storage.

Figure 3 (c) shows the reflectance of SrS and SrS doped zirconium at various precursor temperatures. The spectral analysis reveals that the reflectance of films deposited at 35 °C decreases as the wavelength increases, while those synthesized at 40-45 °C show an increase in reflectance with the wavelength. This could be attributed to the higher precursor temperature. The doped film's high reflectance makes it ideal for photovoltaic applications. The energy bandgap of SrS doped with zirconium at various precursor temperatures is demonstrated in Figure 3 (d). The increase in precursor temperature leads to a decrease in bandgap energy, showing a significant impact on the energy bandgap of SrS doped zirconium [21-25].

The recorded energy bandgap of the synthesized films ranges from 1.50 eV to 1.23 eV.

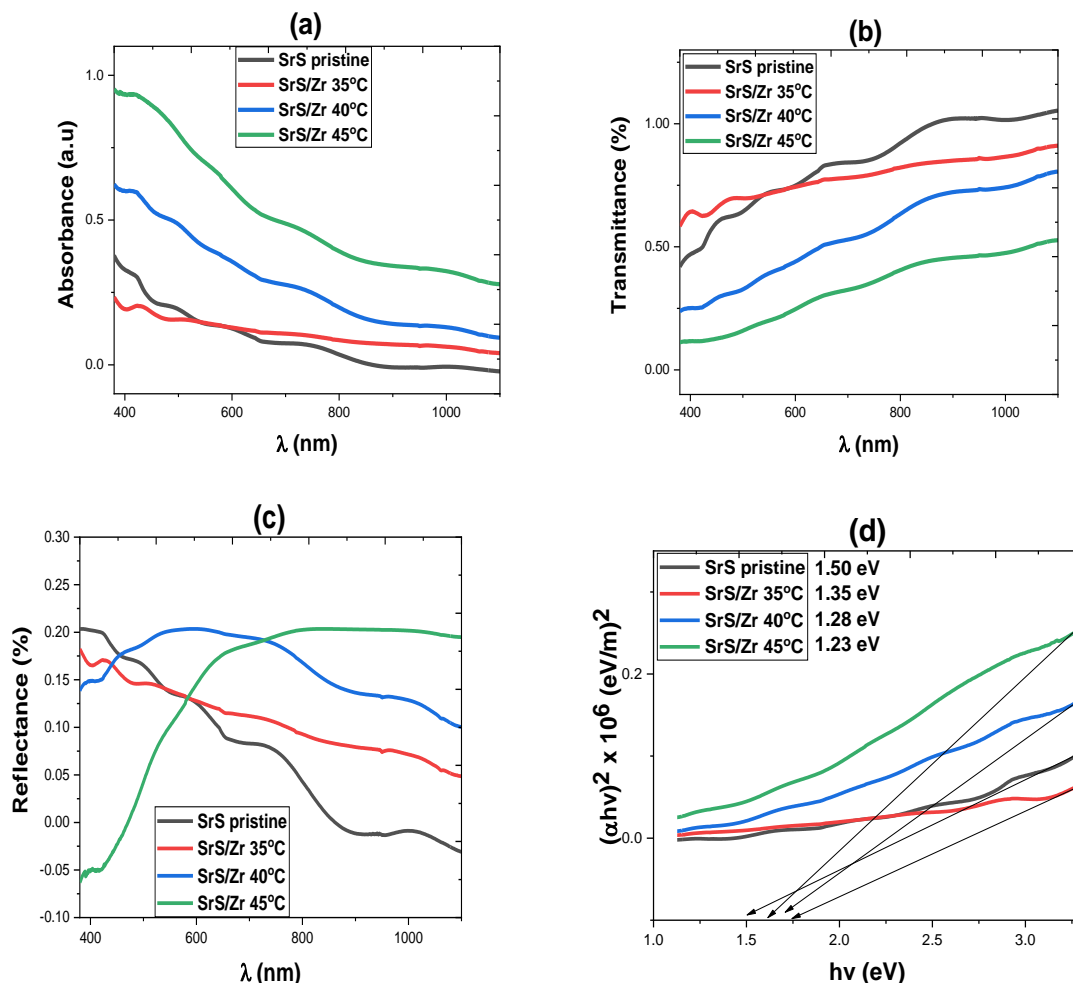


Figure 3: Absorbance (a), transmittance (b), reflectance (c), and energy bandgap (d)

The refractive index, extinction coefficient, and optical conductivity of the films are displayed in Figure 4. In Figure 4 (a), the film without zirconium has a higher refractive index as the photon energy increases. Films with zirconium deposited at higher temperatures have a lower refractive index as photon energy increases. When the films are deposited at a precursor temperature of 350°C, they exhibit the same trend as the undoped SrS films. The plot shows that using the films' refractive index is helpful for photovoltaic and solar cell applications. In Figure 4 (b and c), higher precursor temperature and photon energy lead to increased extinction coefficient and optical conductivity. These films are ideal for solar applications due to their refractive index, extinction coefficient, and optical conductivity.

Figure 5 illustrates the real and imaginary dielectric constant of the synthesized films. Figure 5 (a) illustrates that the real part of the film increases with rising photon energy for the film without zirconium, while films with zirconium deposited at different precursor temperatures exhibit a decrease in response to increasing photon energy. The films deposited at 35 °C follow the same pattern as the undoped SrS films. Based on the spectra, the films' real-part proves to be a superior material for photovoltaic and solar cell applications [26,27]. As the precursor temperature and photon energy increase, the imaginary part in Figure 5(b) also increases. The synthesized films' real and imaginary parts are highly suitable for photovoltaic and solar uses

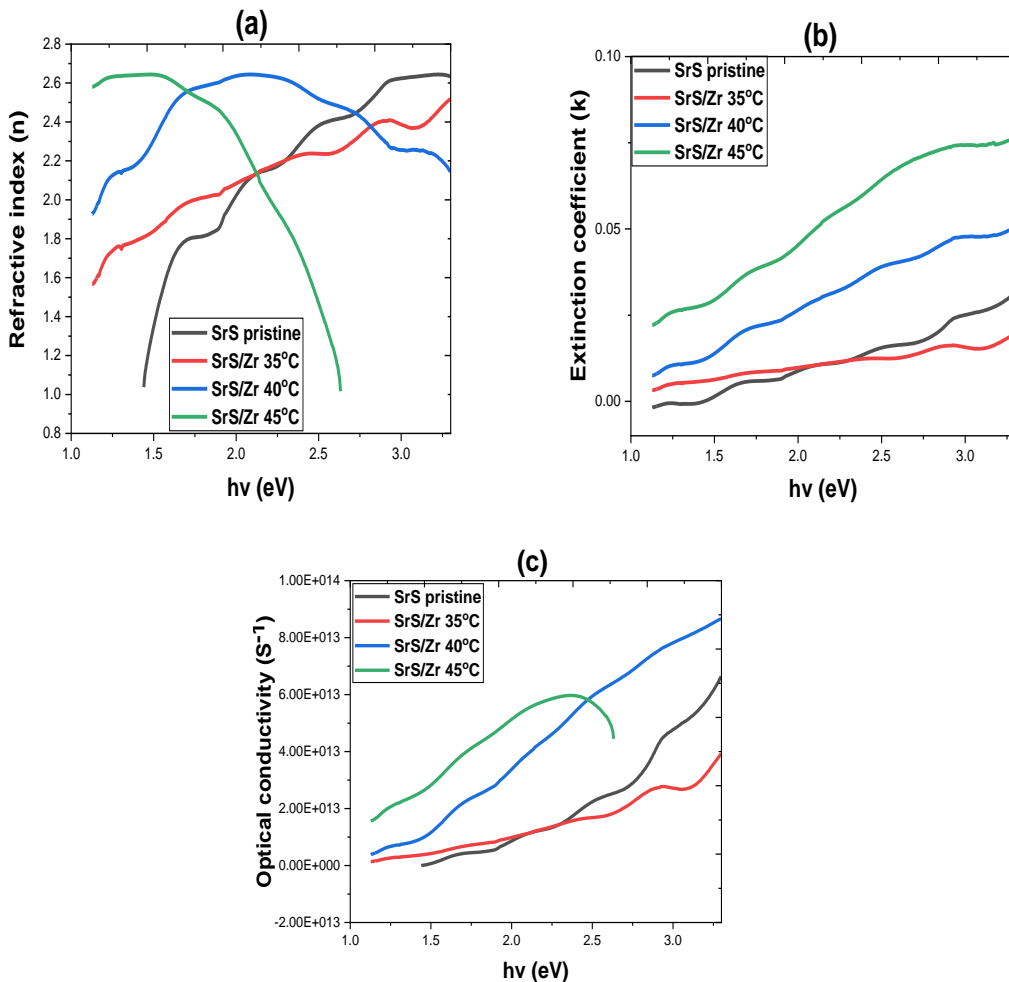


Figure 4: Refractive index (a), extinction coefficient (b), and optical conductivity (c)

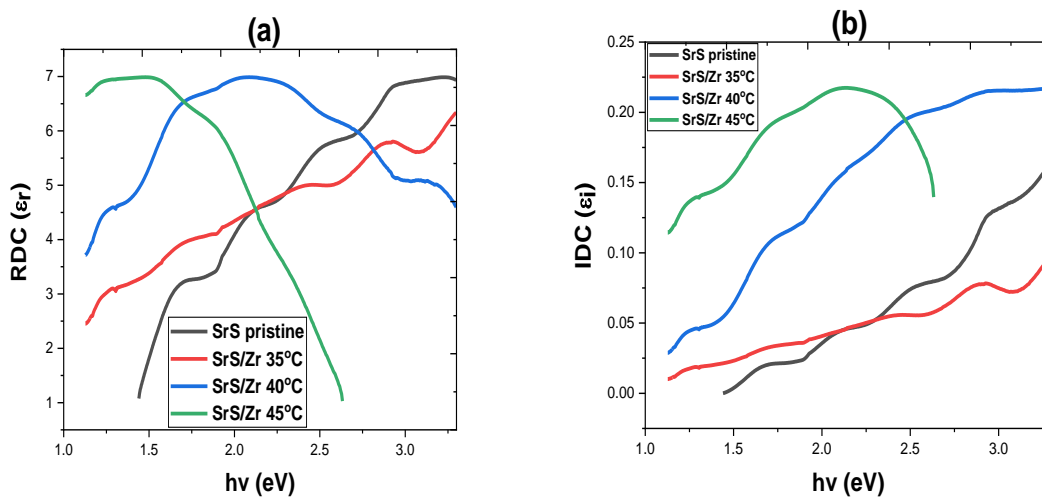


Figure 5: (a) Real, and imaginary dielectric constant (b)

Morphology of SrS and doped SrS on zirconium at various temperatures

The surface micrograph in Figure 6 displays agglomeration on the films without pinholes and small grain size or nanoparticles. The SrS surface morphology displays a Clove-like appearance, with visible precipitate in the SrS micrograph.

Two instances of cloudlike precipitate are observed on the films surface, which is influenced by the precursor temperature. The increase in precursor temperature caused a thick cloud to form on the film surface, caused

by the recirculation of the cloudlike precipitate. Homogeneous deposition of nanoparticles was observed on the entire substrate of the doped SrS material for photovoltaic purposes [24-27]. The zirconium doped films on the FTO substrate have a solid structure with no cracks or lattice strain, making them perfect for electronic applications, including photovoltaics.

In Figure 7, the elemental spectrum of SrS and SrS doped zirconium films is depicted, revealing prominent peaks for strontium, sulphide, and the dopant zirconium. The spectrum shows another element, which is the FTO substrate used in the synthesis.

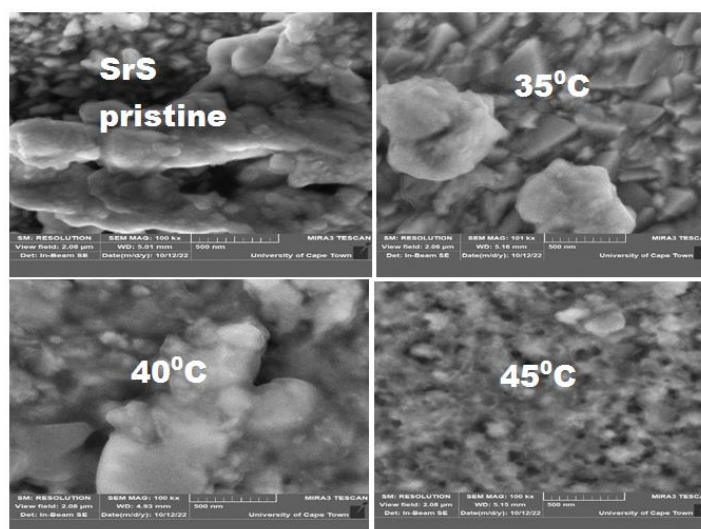


Figure 6: Surface micrograph

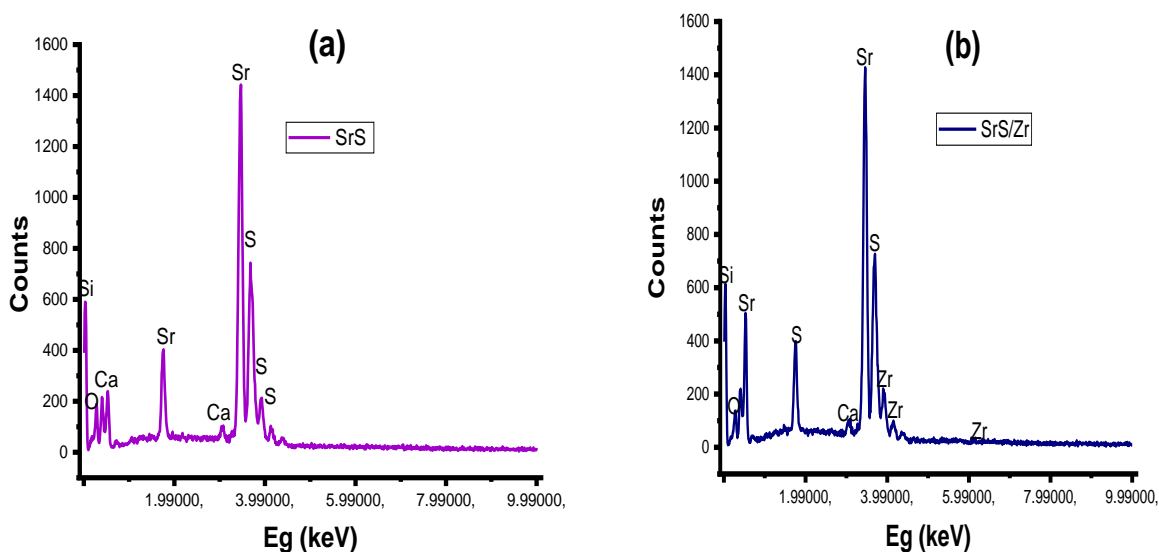


Figure 7: EDX spectrum

Table 3: Atomic weight percentages of the constituent elements in EDX spectra

SrS		SrS doped Silver	
Elements	Atomic Weight (%)	Elements	Atomic Weight (%)
Sr	60.06	Sr	60.37
S	20.02	S	17.00
Si	9.92	Si	9.01
Ca	5.99	Ca	2.60
O	4.01	O	3.00
-	-	Zr	8.01

Conclusion

The electrochemical deposition technique was successfully utilized in growing SrS and SrS/Zr films for photovoltaic applications. The spectrum exhibits a cubic structure, featuring a distinct peak at orientation (111) and a polycrystalline composition. By adding 0.01 mol of zirconium dopant, the peak intensity increases, indicating the acceptance of the dopant by the precursor.

The peak intensity grows with higher precursor temperature, suggesting crystallite formation in the films. The films experience a decrease in thickness from 125.02 to 102.03 nm and an increase in resistivity from 1.31×10^9 to 1.39×10^9 ohm.m, leading to a decline in conductivity from 7.57×10^8 to 7.19×10^8 S/m. The cubic structure of the spectrum is evident, with a distinct peak at orientation (111), and it is polycrystalline. By adding 0.01 mol of zirconium dopant, the peak intensity increases, indicating successful dopant acceptance by the precursor.

The peak intensity of the films grows with higher precursor temperature, indicating crystallite presence. The surface morphology of the films is influenced by the precursor temperature, resulting in a cloudlike precipitate in two instances. With an increase in precursor temperature, the cloudlike precipitate recirculated and created a dense cloud on the film's surface. Homogeneous deposition of nanoparticles on the entire substrate was observed in the doped SrS material, making it suitable for photovoltaic applications. The

recorded energy bandgap of the synthesized films ranges from 1.50 eV to 1.23 eV.

ORCID

Imosobomeh L. Ikhioya : [0000-0002-5959-4427](https://orcid.org/0000-0002-5959-4427)

Reference

- [1]. Y. Chen, S. Fan, G. Gao, *Journal of Physics D: Applied Physics*, **2022**, *55*, 455108. [[Crossref](#)], [[Google Scholar](#)], [[Publisher](#)]
- [2]. M. Kanoğlu, Y.A. Çengel, J.M. Cimbala, *Fundamentals and Applications of Renewable Energy*, McGraw-Hill Education: New York, **2020**. [[Google Scholar](#)], [[Publisher](#)]
- [3]. E. Lisin, D. Shuvalova, I. Volkova, W. Strielkowski, *Sustainability*, **2018**, *10*, 1111. [[Crossref](#)], [[Google Scholar](#)], [[Publisher](#)]
- [4]. T. Geremew, *Journal of 3D Printing and Applications*, **2022**, *1*, 1-24. [[Crossref](#)], [[Google Scholar](#)], [[Publisher](#)]
- [5]. J.H. Seo, E. Swinnich, Y.Y. Zhang, M. Kim, *Materials Research Letters*, **2020**, *8*, 123-144. [[Crossref](#)], [[Google Scholar](#)], [[Publisher](#)]
- [6]. S.J. Sweeney, J. Mukherjee, *Optoelectronic Devices and Materials*. Springer International Publishing AG: Scotland, UK, **2017**, pp. 897-932. [[Crossref](#)], [[Google Scholar](#)], [[Publisher](#)]
- [7]. P. Priyadarshini, S. Das, R. Naik, *RSC Advances*, **2022**, *12*, 9599-9620. [[Crossref](#)], [[Google Scholar](#)], [[Publisher](#)]
- [8]. V. Zaikova, N. Melnikova, A. Tebenkov, A. Mirzorakhimov, O. Shchetnikov, A. Babushkin, G. Sukhanova, *IOP Publishing*, **2017**, *917*, 082009. [[Crossref](#)], [[Google Scholar](#)], [[Publisher](#)]

- [9]. S. Tishkov, A. Scherbak, A. Volkov, V. Karginova-Gubinova, A. Tleppaev, A. Pahomova, Tishkov, S., Shcherbak, A., Karginova-Gubinova, V., Volkov, A., Tleppayev, *Pakhomova*, **2020**, 3354-3368. [[Crossref](#)], [[Google Scholar](#)], [[Publisher](#)]
- [10]. N. Andryeyeva, O. Nikishyna, B. Burkynskyi, N. Khumarova, O. Laiko, H. Tiutiunnyk, *Insights into Regional Development*, **2021**, 3, 198-212. [[Crossref](#)], [[Google Scholar](#)], [[Publisher](#)]
- [11]. M. Ucal, G. Xydis, *Sustainable Cities and Society*, **2020**, 60, 102210. [[Crossref](#)], [[Google Scholar](#)], [[Publisher](#)]
- [12]. A.K. Nasr, M.K. Kashan, A. Maleki, N. Jafari, H. Hashemi, *Entrepreneurship and Sustainability Issues*, **2020**, 7, 2526-2541. [[Crossref](#)], [[Google Scholar](#)]
- [13]. A. Aghahosseini, C. Breyer, *Energy conversion and management*, **2018**, 169, 161-173. [[Crossref](#)], [[Google Scholar](#)], [[Publisher](#)]
- [14]. S.O. Samuel, M.L.-e. Frank, E. Ogherohwo, A. Ekpekpoo, J. Zhimwang, I.L. Ikhioya, *East European Journal of Physics*, **2023**, 189-196. [[Crossref](#)], [[Google Scholar](#)], [[Publisher](#)]
- [15]. I.L. Ikhioya, E.U. Onoh, A.C. Nkele, B.C. Abor, B. Obitte, M. Maaza, F.I. Ezema, *East European Journal of Physics*, **2023**, 162-172. [[Crossref](#)], [[Google Scholar](#)], [[Publisher](#)]
- [16]. I.L. Ikhioya, F.U. Ochai-Ejeh, C.I. Uruwah, *Materials Research Innovations*, **2023**, 1-10. [[Crossref](#)], [[Google Scholar](#)], [[Publisher](#)]
- [17]. I.L. Ikhioya, E.U. Onoh, D.N. Okoli, A.J. Ekpunobi, *Materials Research Innovations*, **2023**, 1-9. [[Crossref](#)], [[Google Scholar](#)], [[Publisher](#)]
- [18]. A.E. Hashim, F.T. Ibrahim, *Chemical Methodologies*, **2023**, 7, 314-324. [[Crossref](#)], [[Publisher](#)]
- [19]. Z.H. Ali, L.A. Abdullah, *Chemical Methodologies*, **2023**, 7, 307-313. [[Crossref](#)], [[Publisher](#)]
- [20]. F. Ali, I. Ahmad, A. Hussain, S. Ahmad, M. Zaka Ansar, Y. Adezuka, I.L. Ikhioya, *Journal of Applied Organometallic Chemistry*, **2023**, 3, 308-320. [[Crossref](#)], [[Publisher](#)]
- [21]. H. Shah, S. Afzal, M. Usman, K. Shahzad, I. Lucky, *Advanced Journal of Chemistry, Section A*, **2023**, 6, 342-351. [[Crossref](#)], [[Google Scholar](#)], [[Publisher](#)]
- [22]. A. Heidari pour, F. Salmani, *Asian Journal of Green Chemistry*, **2024**, 8, 15-24. [[Crossref](#)], [[Publisher](#)]
- [23]. M. Farahmandjou, P. Khalili, *Asian Journal of Green Chemistry*, **2021**, 5, 219-226. [[Crossref](#)], [[Publisher](#)]
- [24]. F. Ibrahim, M.A. Shahoodh, S. Guermazi, *Chemical Methodologies*, **2023**, 7, 871-882. [[Crossref](#)], [[Publisher](#)]
- [25]. I.L. Ikhioya, A.C. Nkele, *Arabian Journal for Science and Engineering*, **2023**, 1-9. [[Crossref](#)], [[Google Scholar](#)], [[Publisher](#)]
- [26]. I.L. Ikhioya, N.I. Akpu, E. Onoh, S.O. Aisida, I. Ahmad, M. Maaza, F. Ezema, *Journal of Medicinal and Nanomaterials Chemistry*, **2023**, 5, 156-167. [[Crossref](#)], [[Publisher](#)]
- [27]. K.I. Udofia, I.L. Ikhioya, D.N. Okoli, A.J. Ekpunobi, *Journal of Medicinal and Nanomaterials Chemistry*, **2023**, 5, 135-147. [[Crossref](#)], [[Publisher](#)]

Copyright © 2023 by SPC ([Sami Publishing Company](#)) + is an open access article distributed under the Creative Commons Attribution License(CC BY) license (<https://creativecommons.org/licenses/by/4.0/>), which permits unrestricted use, distribution, and reproduction in any medium, provided the original work is properly cited.